ACS OMEGA

Open Access

http://pubs.acs.org/journal/acsodf

Article

Modeling and Optimization of Modified TiO_2 with Aluminum and Magnesium as ETL in $MAPbI_3$ Perovskite Solar Cells: SCAPS 1D Frameworks

Abdullahi Usman and Thiti Bovornratanaraks*

Cite This: *ACS Omega* 2024, 9, 39663−39672

Read Online

ACCESS | Metrics & More | Article Recommendations | Supporting Information

ABSTRACT: The perovskite device, incorporating a modified nanostructure of TiO_2 as the electron transport layer, has been investigated to enhance its performance compared to the pure TiO_2 device. Various materials undergo electrochemical doping or treatment on TiO_2 to improve their photocatalytic application, thereby enhancing the current density, minimizing recombination, and improving device stability. In this study, a numerical SCAPS simulation was employed to validate experimental findings from the literature. According to the literature, this marks the first instance of doping Al^{3+} and Mg^{2+} on TiO_2 due to their ionic radius comparable to that of Ti^{4+}, at different doping concentrations. The device was modeled and simulated with the experimental parameters of bandgap, series, and shunt resistances for pure TiO_2, aluminum-doped TiO_2 (Al-TiO_2), and magnesium-doped TiO_2 (Mg-TiO_2). From the validated results, the Al-TiO_2 and Mg-TiO_2-based devices' configurations with minimum percentage errors of 0.427 and 2.771%, respectively, were selected and simulated across nearly 90 (90) configurations to determine the optimum device model. Optimizing absorber thickness, bandgap, doping concentration, metal electrode, as well as series and shunt resistance resulted in enhanced device performance. According to the proposed model, Al-TiO_2 and Mg-TiO_2 configurations achieved higher power conversion efficiency values of 19.260 and 19.860%, respectively. This improvement is attributed to the reduction in recombination rates through the injection of a higher photocurrent density.

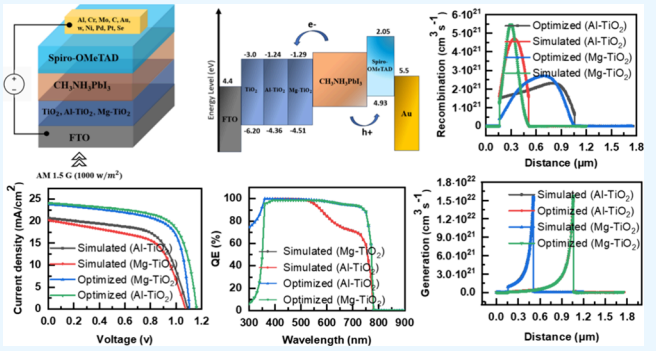

1. INTRODUCTION

The performance evaluation of perovskite devices is receiving significant attention in the field of solar cells. This attention is attributed to their excellent charge transport properties, and high absorption coefficient, which help minimize defects such as recombination. As a result, perovskite solar cells exhibit high photoconversion efficiency (PCE) and are considered suitable for low-cost production.[1−3] For almost a decade, SCAPS numerical simulation has gained global recognition as one of the best and most straightforward methods for assessing perovskites in various configurations, including different tunable bandgaps, thicknesses, and other essential material characterizations. These evaluations would otherwise be challenging, inefficient, and costly to perform through experimental benchmarks.[4−7] It has been established that semiconductor-based TiO_2 stands out as one of the most promising candidates for serving as the (ETL) in perovskite devices.[8−13] Due to its nanocrystalline structure, it easily undergoes modification, electrochemical doping, or treatment with other materials, resulting in various applications. These applications include photocatalytic processes[14−16] and water splitting, contributing to enhancements in photocurrent density, stability, and device operation at low temperatures.[15,17,18] Hence, the performance of both doped and undoped TiO_2 is examined to evaluate the potential improvements brought about by the treatment of TiO_2 compared with its untreated counterparts. The treatment with TiO_2 resulted in a band offset, leading to enhanced band alignment. This band alignment is crucial as it can minimize recombination defects, thereby improving the flow of charge carriers and ultimately enhancing device performance.[19] Various materials, such as magnesium (Mg), neodymium (Nd), samarium (Sm), cobalt (Co), lithium (Li), and zinc (Zn), have been synthesized and applied as dopants to TiO_2. This doping process, achieved through experimental fabrication using the solvothermal method[20] or computational methods in density functional theory,[21] aims to reduce the electronic trap density,

Received: May 12, 2024
Revised: August 31, 2024
Accepted: September 3, 2024
Published: September 12, 2024

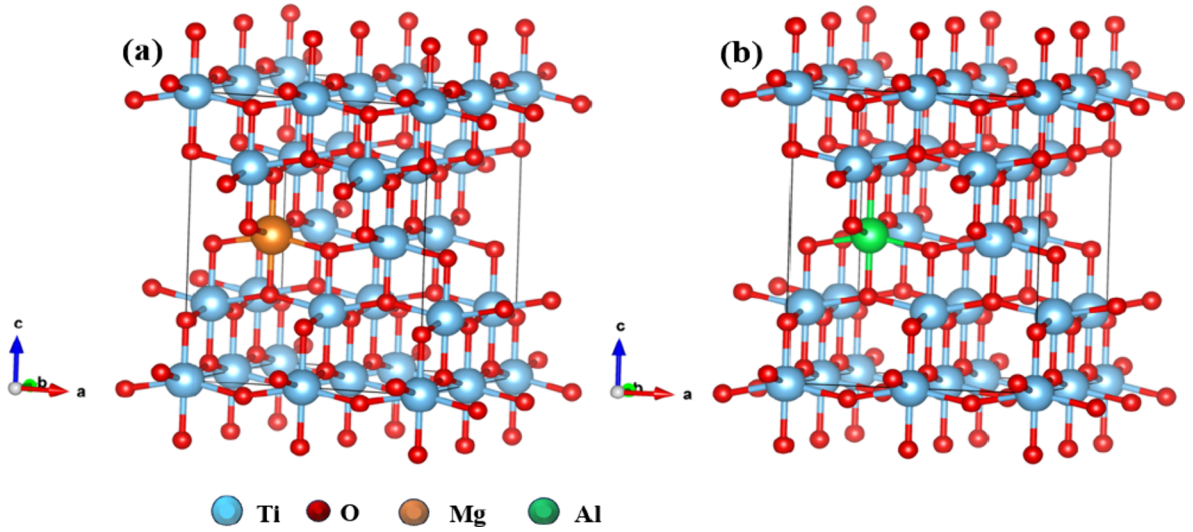

Figure 1. Illustration showing anatase (101) TiO_2 supercell lattice structure resulted from the doping of (a) Mg^{2+} and (b) Al^{3+}.[31]

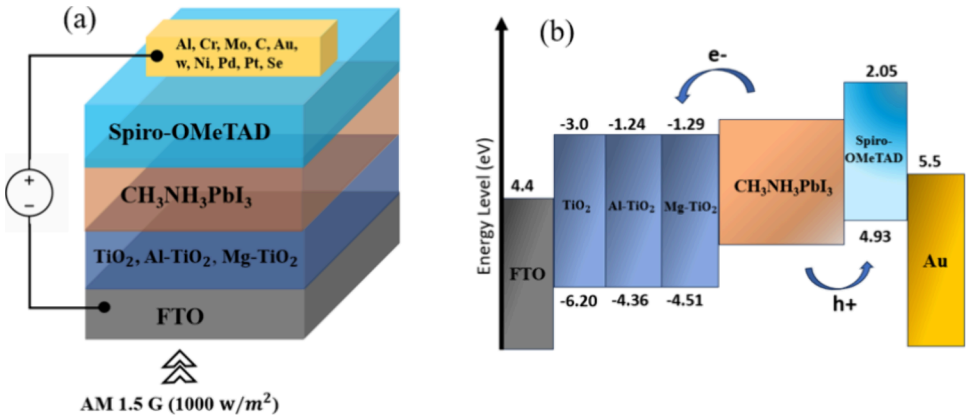

Figure 2. (a) Schematic diagram and (b) energy band alignment of the device configuration.

consequently enhancing electron transport within the device.[8,22−25]

Several studies have studied the doping characteristics of Al and Mg materials on TiO_2, which resulted in the TiO_2 band alignment for magnetic and nanostructural properties.[22,26−30] According to Figure 1, for the first time in ref 31, anatase TiO_2 has been successfully modified through the doping of Al^{3+} and Mg^{2+} ions. This achievement is attributed to their comparable ionic radii to that of Ti^{4+}, achieved at various doping concentrations using the sol−gel method. The lattice structure, morphological view, and particle size were subsequently calculated and analyzed successfully. The doping overcomes the oxygen vacancies, offsets the bandgap, reduces the surface and trap states, and decreases the electron−hole recombination rate, which enhances the electron mobility, FF, and electron transport, resulting in an overall increase in device performance. However, it has been observed that some crucial measurements must be rechecked for their influence on the device's performance, as obtained in ref 31. The values of various series resistance (R_s) and shunt resistances (R_{sh}) across the device configuration affect the flow of the current. The performance of the perovskite device is contingent upon the quality of individual layers, the absorber bandgap, doping concentration, and absorber thickness, all of which play a vital role in minimizing the recombination of electrons. Additionally, the exploration of various abundant metals suitable for the electrode at the back contact, with a well-defined work function and low cost, is preferred, as it also plays a crucial role in the device's performance.

Here, we simulated a perovskite device in SCAPS using experimental parameters from ref 31 to validate results obtained by tuning the electrical and structural properties of pure TiO_2 and doped TiO_2 with Al and Mg as the ELT. The various tests outlined were designed to achieve optimum performance.[32,33] The discussion is organized into three main sections. In the first section, the SCAPS model was simulated at various doping concentrations, considering exact R_s and R_{sh} values from ref 31. This validation process aimed to minimize the percentage error and ensure an accurate representation of the device's performance. Subsequently, in the second section, configurations with the least error were chosen as references for device optimization. The focus was on minimizing recombination rates and enhancing the overall performance. Parameters, such as optimized bandgap, operating temperature, R_s/R_{sh} resistance, and absorber doping concentration, were fine-tuned to match experimental values. Additionally, absorber thickness optimization, which directly influences recombination, was addressed. Moreover, different device configurations were tested with various metal electrodes, each having different work function values. This exploration

https://doi.org/10.1021/acsomega.4c04505
ACS Omega 2024, 9, 39663−39672

Table 1. Simulation Parameters for the Perovskite Device Configuration

parameters	FTO[36]	TiO_2[37]	SpiroOMeTAD[13]	Al- TiO_2[37]	Mg-TiO_2[37]	$CH_3NH_3PbI_3$[36]
thickness (nm)	660	20.7[31]	160	17.1, 22, 24.2[31]	19, 22.7[31]	350
bandgap, (eV)	3.5	3.2[31]	3.0	3.12[31]	3.22[31]	1.6
electron affinity, (eV)	4.0	4.2	2.45	4.2	4.2	4.0
dielectric permittivity, ε_r	9.0	10	3.0	13.6[13]	13.6[13]	9.0
CB effective density of states, N_C (cm^{-3})	2.2×10^{19}	2.2×10^{18}	2.5×10^{18}	2.2×10^{18}	2.2×10^{18}	2.2×10^{18}
VB effective density of states, N_V (cm^{-3})	2.2×10^{19}	2.2×10^{18}	1.8×10^{19}	2.2×10^{18}	2.2×10^{18}	2.2×10^{19}
electron mobility, μ_n ($cm^2\ V^{-1}\ S^{1-}$)	20.0	20.0	2×10^{-4}	20	20	2.0
hole mobility, μ_h ($cm^2\ V^{-1}\ S^{1-}$)	20.0	10.0	2×10^{-4}	10	10	2.0
acceptor density, N_A (cm^{-3})	0.0	0.0	1×10^{18}	0.0	0.0	1×10^{13}
donor density, N_D (cm^{-3})	1×10^{19}	1×10^{17}	0.0	1×10^{17}	9×10^{20}	0.0
defect density, N_t (cm^{-3})	1×10^{15}	1×10^{15}	1×10^{15}	1×10^{15}	1×10^{15}	3×10^{15}

Table 2. Performance Comparison of the Validated Result with Simulation Model and Experimental Research in Ref 31

				V_{oc} (V)		J_{sc} (mA/cm^2)		FF (%)		PCE (%)		
ETL (mol %)[31]	thickness (nm)[31]	R_{sh} ($\Omega\ cm^2$)[31]	R_s ($\Omega\ cm^2$)[31]	experiment[31]	this work	experiment[31]	this work	experiment[31]	this work	experiment[31]	this work	error in PCE (%)
pure TiO_2	20.7	254	10.0	1.00	1.10	18.62	17.25	61.80	59.46	11.49	11.32	1.47
Mg-TiO_2(0.1)	22.7	201	6.1	1.06	1.07	19.22	20.24	60.10	57.95	12.27	12.61	2.77
Mg-TiO_2(0.5)	19.0	227	6.6	1.06	1.08	19.00	20.26	60.70	58.93	12.24	12.87	5.15
Mg-TiO_2(1.0)	22.7	267	5.3	1.02	1.08	17.34	20.45	60.40	61.75	10.64	13.65	28.28
Al-TiO_2(0.1)	24.2	326	7.4	1.06	1.09	19.79	20.64	61.00	60.66	12.77	13.68	7.13
Al-TiO_2(0.5)	17.1	330	6.4	1.07	1.09	20.86	20.71	63.00	61.81	14.05	13.99	0.43
Al-TiO_2(1.0)	22.0	353	6.8	1.07	1.09	20.57	20.71	62.80	61.85	13.88	14.01	0.94

aimed to assess the possibility of replacing the nickel (Ni) metal electrode in the original configuration based on considerations of conductivity, cost, and availability. In the final section of this article, we present the optimized device configuration, providing a performance comparison between the simulated and optimized devices.

2. MODELING SIMULATION OF THE PEROVSKITE SOLAR CELLS

The perovskite device is modeled in SCAPS using Poisson's and continuity equations as the fundamental starting equations. The Poisson describes the electrostatic potential of the overall charge density, whereas the continuity equation determines the solar cell quality attributes to the electrons and holes.[5,6] Poisson's and continuity equations of electrons and holes are given in eqs 1−3, respectively:

$$\nabla^2\psi = q/\varepsilon(n - p + N_A - N_D) \quad (1)$$

$$\nabla J_n - q\frac{\partial n}{\partial t} = +qR \quad (2)$$

$$\nabla J_p + q\frac{\partial p}{\partial t} = -qR \quad (3)$$

where ψ is the electrostatic potential, N_A and N_D are the donor and acceptor concentration of the electron (n) and hole (p), respectively, ε is the dielectric permittivity of the medium, q is the electron charge, R is the carrier recombination, and J_n and J_p represent the electron and hole current densities, respectively.

According to the schematic diagram depicted in Figure 2a and the simulation parameters presented in Table 1 of the device configuration, the perovskite device is modeled in SCAPS by utilizing a lead-based perovskite absorber, specifically $CH_3NH_3PbI_3$ ($MAPbI_3$), known for its convenience and high performance[34,35] with the Spiro-OMeTAD as the hole transport layer. The device follows the experimental configuration of FTO/TiO_2/$CH_3NH_3PbI_3$/Spiro-OMeTAD/Ni, as published in ref 31, with the connection made through a Ni metal electrode at the back contact. This illustration includes three structural investigations of the electron transport layer (ELT) of TiO_2, specifically Al-TiO_2 and Mg-TiO_2. The standard spectrum of the AM 1.5G with 1000 W/m^2 is set to simulate the n-i-p model by illumination at the FTO surface area at the default operating temperature of 300 K. The three configurations are simulated using the respective experimental bandgap values of 3.2, 3.22, and 3.12 eV as depicted in Figure 2b, along with the series and resistance values. Seven configurations were simulated to validate the experimental findings. In addition, almost 90 configurations were tested for device optimization. This involved varying the absorber thickness, absorber doping concentration, R_s and R_{sh}, operating temperature parameters, and metal electrodes at various work functions. These variations were chosen within the experimental values to ensure a comprehensive exploration. Finally, the optimized device is configured with the help of all of the optimized parameters, and its performance is compared to that of the original device.

https://doi.org/10.1021/acsomega.4c04505
ACS Omega 2024, 9, 39663−39672

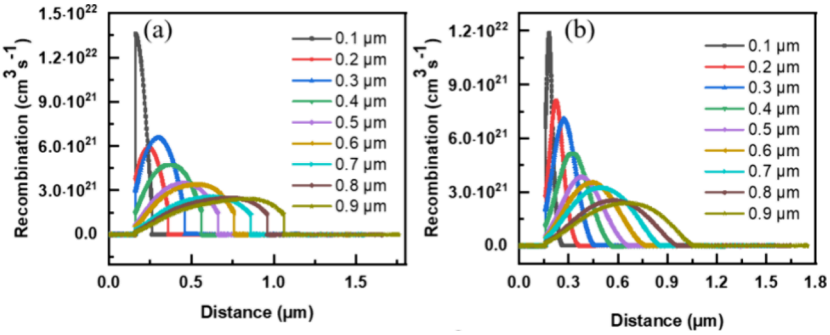

Figure 3. Effect of recombination at various absorber thickness of (a) Al-TiO_2 and (b) Mg-TiO_2.

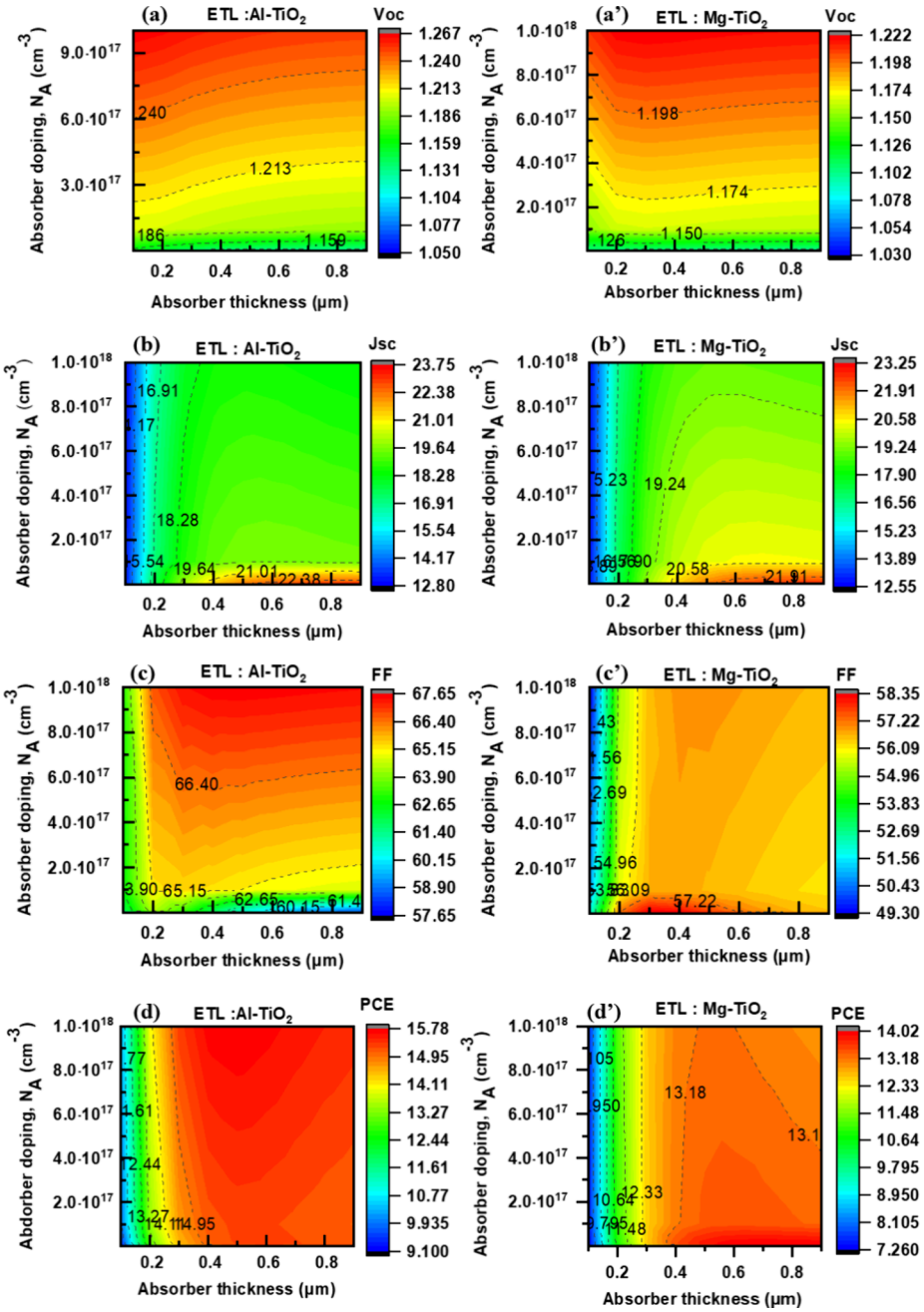

Figure 4. Contour mapping of perovskite device performance parameters while (a and a') represent V_{oc}, (b and b') represent J_{sc}, (c and c') represent FF, and (d and d') represent the PCE depending on the absorber thickness and absorber doping concentration with ETL Al-TiO_2 and Mg-TiO_2.

https://doi.org/10.1021/acsomega.4c04505
ACS Omega 2024, 9, 39663−39672

3. RESULT AND DISCUSSIONS

3.1. Validation of the Experimental Result Using a Proposed Model. Table 2 presents a performance comparison between simulated and experimental results published in ref 31 for pure TiO_2, Mg-TiO_2, and Al-TiO_2 under varying R_s/R_{sh} and different doping concentrations ranging from 0.1 to 1 mol %. FF and PCEs demonstrated a direct proportional increase with higher doping concentrations, while open-circuit voltages (V_{oc}) and short-current densities (J_{sc}) exhibited minimal changes. These findings align well with the experimental values reported in the literature. In terms of PCE comparison, minimum percentage errors were observed in pure TiO_2. Conversely, Mg-TiO_2 and Al-TiO_2 of thickness values of 22.7 and 17.1 nm exhibited minimum percentage errors of 2.77 and 0.43%, respectively, at the lowest R_s/R_{sh} of 6.1/201 and 6.4/330 Ω cm^2. Consequently, these specific parameters were selected as reference values for the active perovskite configuration to carry out other analyses for optimizing device performance.

3.2. Effect of an Absorber Doping Concentration. According to ref 3, an increase in absorber doping concentration improves efficiency by enhancing the built-in electric field, thereby facilitating charge carrier separation. Table S1.a showcases the performance of Al-TiO_2-based devices at various absorber doping levels, ranging from 10^{14} to 10^{18} cm^{-3}. The V_{oc} and FF demonstrated an upward trend with increasing doping concentration, leading to a higher PCE value at 10^{18} cm^{-3}, a doping value experimentally accepted.[38] However, the J_{sc} experienced a decrease due to the scattering effect. Conversely, the Mg-TiO_2-based device exhibited superior performance at a doping concentration of 10^{16} cm^{-3} as detailed in Table S1.b. Figure 3 illustrates contour mapping of perovskite device performance parameters while (a and a') represent V_{oc}, (b and b') represent J_{sc}, (c and c') represent FF, and (d and d') represent the PCE depending on the absorber thickness and absorber doping concentration with ETL Al-TiO_2 and Mg-TiO_2.As depicted in Figure 4, the Al-TiO_2-based device outperformed the Mg-TiO_2-based device in terms of FF and PCE, while V_{oc} remained nearly the same. Notably, the J_{sc} significantly decreased in both devices. The V_{oc}, J_{sc}, FF, PCE, as well as *JV* curves of the perovskite device at various absorber doping concentrations with ETL (a) Al-TiO_2 and (b) Mg-TiO_2 are presented in Figures S1 and S2.

3.3. Optimized Thickness at the Minimum Recombination Rate. Several research studies have been conducted to investigate recombination minimization by varying different parameters to enhance device performance.[25,39,40] The device performance using ELT configurations of Al-TiO_2 and Mg-TiO_2, respectively, is analyzed, with absorber thicknesses ranging from 0.1 to 0.9 μm in increments of 0.1. According to Table S2.a, the PCE and J_{sc} values significantly increase as the thickness values increase, while FF fluctuates, and V_{oc} remains almost constant with negligible changes. Conversely, a similar performance trend is observed in Mg-TiO_2 in Table S2.b, but the PCE slightly drops from 0.8 μm. Figure S3 illustrates *JV* curves at various absorber thicknesses with the ELT layer of (a) Al-TiO_2 and (b) Mg-TiO_2. In both devices, the highest PCE is achieved at a thickness value of 0.6 μm, while the highest current densities are realized at thickness values of 0.9 μm. Therefore, based on ref 15, the larger J_{sc} can be attributed to faster electron transfer, resulting in reduced recombination effects. Thus, the optimized absorber thickness for both configurations is 0.9 μm. Figure 4 contours mapping of perovskite device performance parameters while (a and a') represent V_{oc}, (b and b') represent J_{sc}, (c and c') represent FF, (d and d') represent the PCE depending on the absorber thickness and absorber doping concentration with ETL Al-TiO_2 and Mg-TiO_2. Figure 3 illustrates the effect of recombination at various absorber thicknesses of (a) Al-TiO_2, and (b) Mg-TiO_2. According to Figure 4a,b, the highest recombination is observed at 0.1 μm before dropping to the lowest recombination at 0.9 μm.

3.4. Effect of Series and Shunt Resistances. *3.4.1. Effect of Series Resistances.* The series resistance (R_s) refers to the solar cell resistance of charge generation, encompassing bulk layers, electrodes, and interface resistance.[38] Table 3 presents

Table 3. Perovskites Performance at Various Series Resistances with ETL (Al-TiO_2)

R_s (Ω cm^2)	V_{oc} (V)	J_{sc} (mA/cm^2)	FF (%)	PCE (%)
default	1.093	21.121	68.688	15.851
2	1.093	20.991	66.529	15.260
4	1.093	20.863	64.390	14.680
6	1.093	20.735	62.241	14.104
8	1.093	20.609	60.101	13.537
10	1.093	20.484	57.977	12.980

the performance of R_s ranging from the default value (0) to 10 Ω cm^2 in the device configuration of FTO/Al-TiO_2/$CH_3NH_3PbI_3$/Spiro-OMeTAD/Ni, with a constant shunt resistance (R_{sh}) value of 330 Ω cm^2. As the R_s of the device increases from 0 to 10 Ω cm^2, the fill factor (FF) decreases due to solder bond degradation, resulting in a decrease in PCE due to power loss. However, J_{sc} slightly decreases, indicating minimal optical transmission loss due to discoloration, while V_{oc} remains unchanged. These results are in good agreement with those obtained in ref 23. On the other hand, the R_{sh} value of 201 Ω cm^2 remains constant while R_s varies from 0 to 10 Ω cm^2 in the FTO/Mg-TiO_2/$CH_3NH_3PbI_3$/Spiro-OMeTAD/Ni configurations. According to Table 4, the same trends in V_{oc},

Table 4. Device Performance at Various Series Resistances with ETL (Mg-TiO_2)

R_{sh} (Ω cm^2)	V_{oc} (V)	J_{sc} (mA/cm^2)	FF (%)	PCE (%)
default	1.075	20.863	62.647	14.055
2	1.075	20.654	61.146	13.581
4	1.075	20.450	59.598	13.106
6	1.075	20.249	58.030	12.636
8	1.075	20.052	56.447	12.172
10	1.075	19.858	54.855	11.715

J_{sc}, FF, and PCE are observed. Therefore, lower R_s, preferably the default value (0), would positively affect the solar cell's performance.[34] Consequently, the optimized R_s values for both configurations will be set to the default values in the model. Figure 5a,b illustrates the V_{oc}, J_{sc}, FF, and PCE plots of various R_s for perovskite configurations FTO/Al-TiO_2/$CH_3NH_3PbI_3$/Spiro-OMeTAD/Ni and FTO/Mg-TiO_2/$CH_3NH_3PbI_3$/Spiro-OMeTAD/Ni, respectively. However, the R_s is inversely proportional to the device's J_{sc} and FF, leading to a significant drop in PCE.

3.4.2. Effect of Shunt Resistances. Shunt resistance refers to the solar cell's resistance to recombination. Table 5 presents

https://doi.org/10.1021/acsomega.4c04505
ACS Omega 2024, 9, 39663−39672

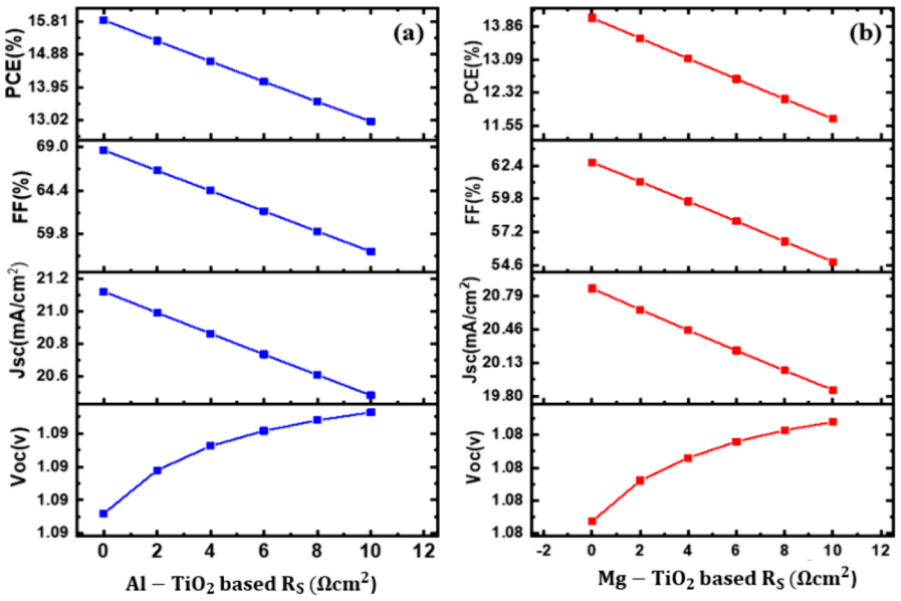

Figure 5. V_{oc}, J_{sc}, FF, and PCE plots of various series resistance of the perovskites with ETL of (a) FTO/Al-TiO_2/$CH_3NH_3PbI_3$/Spiro-OMeTAD/Ni and (b) FTO/Mg-TiO_2/$CH_3NH_3PbI_3$/Spiro-OMeTAD/Ni.

Table 5. Perovskites Performance at Various Shunt Resistances with ETL(Al-TiO_2)

shunt resistance (Ω cm^2)	V_{oc} (V)	J_{sc} (mA/cm^2)	FF (%)	PCE (%)
100	1.064	19.842	44.554	9.405
150	1.079	20.248	52.869	11.553
200	1.086	20.457	57.006	12.663
250	1.090	20.585	59.465	13.337
300	1.092	20.671	61.082	13.786
350	1.093	20.733	62.228	14.107
400	1.095	20.779	63.083	14.348
450	1.095	20.816	63.745	14.536
500	1.096	20.845	64.273	14.686
550	1.097	20.869	64.704	14.809

the performance distribution of the device configuration FTO/Al-TiO_2/$CH_3NH_3PbI_3$/Spiro-OMeTAD/Ni at a fixed R_s of 6.4 Ω cm^2 and varied R_{sh} ranging from 100 to 550 Ω cm^2. As R_{sh} increases, the FF rises, leading to an increase in PCE, with little effect on V_{oc} (open-circuit voltage) and J_{sc} (short-circuit current). In contrast, Table 6 presents the device performance configuration of the FTO/Al-TiO_2/$CH_3NH_3PbI_3$/Spiro-OMeTAD/Ni structure. The R_s of 6.1 Ω cm^2 is kept constant while the shunt resistance is varied from 100 to 550 Ω cm^2. The

Table 6. Device Performance at Various Shunt Resistances with ETL (Mg-TiO_2)

shunt resistance (Ω cm^2)	V_{oc} (V)	J_{sc} (mA/cm^2)	FF (%)	PCE (%)
100	1.049	19.655	45.076	9.294
150	1.067	20.039	53.667	11.474
200	1.075	20.236	57.889	12.596
250	1.080	20.357	60.357	13.270
300	1.083	20.438	61.969	13.720
350	1.086	20.496	63.133	14.047
400	1.087	20.540	63.977	14.288
450	1.089	20.574	64.629	14.476
500	1.090	20.602	65.146	14.626
550	1.091	20.624	65.568	14.748

effects on V_{oc}, J_{sc}, FF, and PCE are like those in Table 5. Figures 6a and 5b illustrate the perovskite performance of FF

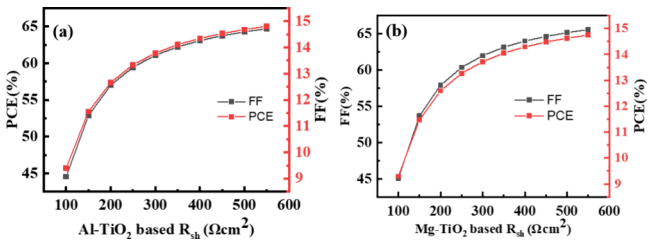

Figure 6. Perovskites performance at various shunt resistances: (a) FTO/Al-TiO_2/$CH_3NH_3PbI_3$/Spiro-OMeTAD/Ni and (b) FTO/Mg-TiO_2/$CH_3NH_3PbI_3$/Spiro-OMeTAD/Ni.

and PCE against various R_{sh} for FTO/Al-TiO_2/$CH_3NH_3PbI_3$/Spiro-OMeTAD/Ni and FTO/Mg-TiO_2/$CH_3NH_3PbI_3$/Spiro-OMeTAD/Ni, respectively. According to both figures, as R_{sh} increases, FF and PCE exponentially rise until they reach a peak point at a higher shunt resistance. This indicates that the device performance increases with higher R_{sh}. Therefore, based on this research, the optimized R_{sh} values for both configurations are 550 Ω cm^2.

3.5. Device Performance at Various Operating Temperatures. According to ref 23, an increase in operating temperature induces deformation stress, leading to a forward movement that increases defect density in the layer. This influences the diffusion length, resulting in a loss of efficiency loss. The device performance at various operating temperatures is configured with ETLs of Al-TiO_2 and Mg-TiO_2, ranging from 270 to 330 K in 10 K increment. In Table S3.a,b, detailing the device performance with the ETL layer of Al-TiO_2, it is observed that V_{oc}, FF, and PCE increase as the operating temperature decreases. There is a slight increase in the level of J_{sc}. The highest FF and PCE values of 62.6127 and 14.9232% are achieved at 270 K, while the lowest values are 60.7977 and 12.984%, respectively. Conversely, Mg-TiO_2 focusing on electrical outputs such as V_{oc} and PCE decrease.

https://doi.org/10.1021/acsomega.4c04505
ACS Omega 2024, 9, 39663−39672

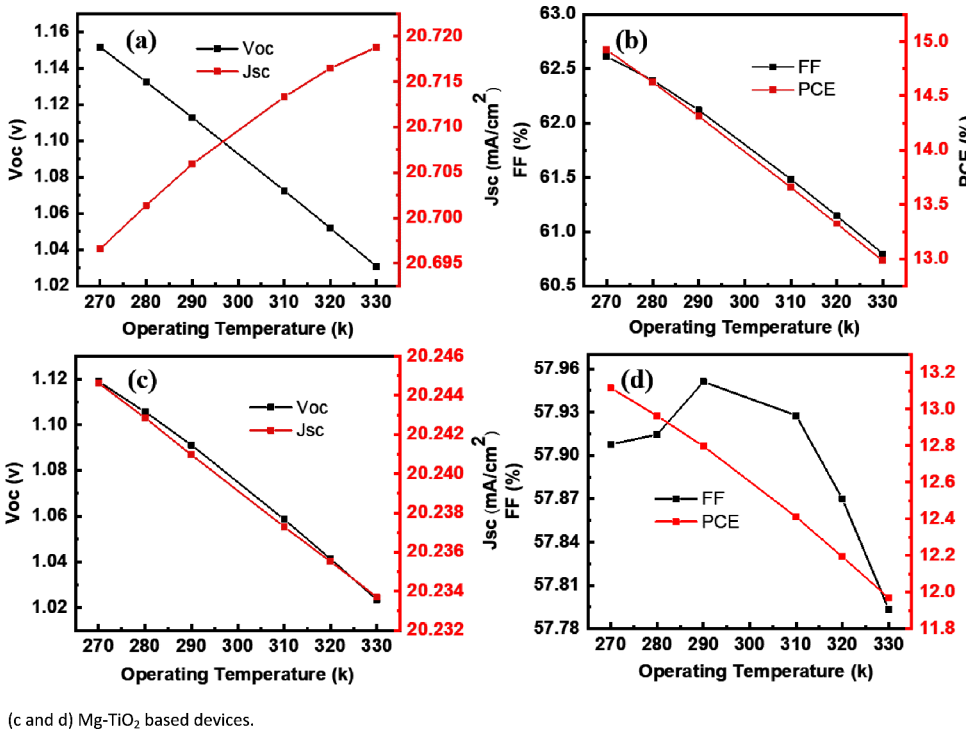

Figure 7. V_{oc}, J_{sc}, FF, and PCE plots against operating temperature ranging from 270 to 330 of (a and b) Al-TiO_2 and (c and d) Mg-TiO_2 based devices.

Table 7. Perovskites Device Performance at Various Metal Back Contacts with ETL (Al-TiO_2 and Mg-TiO_2)

metal electrode	Fe	C	Au	W	Ni	Pd	Pt	Se
work function (eV)	4.81	5.00	5.10	5.22	5.50	5.60	5.70	5.90
Al-TiO_2–PCE (%)	10.911	14.410	16.249	18.294	18.858	18.859	18.859	18.859
Mg-TiO_2–PCE (%)	10.396	13.833	15.629	17.625	18.173	18.174	18.174	18.174

However, J_{sc} and FF remain nearly constant before slightly decreasing. This trend is consistent across the temperature range of 270 to 330 K compared to Al-TiO_2. In both devices with different ETLs, optimal performance is consistently achieved at the operating temperature of 270 K. This result corroborates the optimized operating temperature achieved using the TiO_2 ETL layer, as reported in ref 41. Figure 7a–d shows the performance comparison plots of V_{oc}, J_{sc}, FF, and PCE against the operating temperature range of 270 to 330 K for both Al-TiO_2 and Mg-TiO_2.[42] As depicted in Figure 7a, for the Al-TiO_2 based device, the J_{sc} increases significantly while the V_{oc} decreases with rising temperature, leading to a notable drop in FF and overall performance, as shown in Figure 7b, which is in good agreement with the findings in ref 43. In contrast, Figure 7c shows that both V_{oc} and J_{sc} of the Mg-TiO_2 device decrease significantly as the operating temperature increases as noted in ref 42. Consequently, the decrease in J_{sc} results in a lower FF, which is about 57.91% at 270 K before peaking at around 57.96%, and then slightly dropping at 330 K. This variation leads to a lower PCE in the Mg-TiO_2 device compared to the Al-TiO_2 device over the same temperature range of 270–330 K, which is in good agreement with values presented in Table S3.a,b.

3.6. Device Performance at Various Metal Electrodes. According to the comprehensive overview of the role of the metal electrode in perovskite solar cells presented in refs 37,44, the stability of perovskites is closely linked to the selection of electrode types, influencing overall device performance. The reflection from electrodes and their light-trapping properties contribute to enhancing the device performance. The impact of device recombination using various metal electrodes with different work functions was investigated in configurations based on both Al-TiO_2 and Mg-TiO_2. Table 7 presents the device performance of metal electrodes such as Cr, Mo, C, Au, W, Ni, Pd, Pt, and Se, along with their respective work functions[45] placed at the back contact of FTO/Al-TiO_2/$CH_3NH_3PbI_3$/Spiro-OMeTAD/Ni, as detailed in Table S4.a. The increase in the work functions of the metal electrodes results in improved device performance and vice versa. The lowest PCE of 5.350% is observed with Cr, which is more cost-effective but less stable. Conversely, equal PCE values of >18% are achieved with W, Ni, Pd, Pt, and Se. In Table S4.b, for the FTO/Mg-TiO_2/$CH_3NH_3PbI_3$/Spiro-OMeTAD/Ni structure, the lowest PCE of 6.57% is recorded with the Mo metal electrode, while equal highest PCE values above 18% are observed for W, Ni, Pd, Pt, and Se. Analyzing *JV* curves and efficiency plots of the Al-TiO_2 and Mg-TiO_2 configurations depicted in Figures 8a,d, and 9 respectively, the Ni electrode exhibits a higher *JV* curve and minimum recombination rate compared to other electrodes. Additionally, Ni proves to be the most suitable electrode due to its low cost and abundance, as reported in ref 46.

3.7. Overall Performance of Experimental Devices and Proposed Models of Al-TiO_2 and Mg-TiO_2. The perovskite device was analyzed with various absorber bandgap configurations ranging from 1.3 to 1.65 eV. The Al-TiO_2

https://doi.org/10.1021/acsomega.4c04505
ACS Omega 2024, 9, 39663–39672

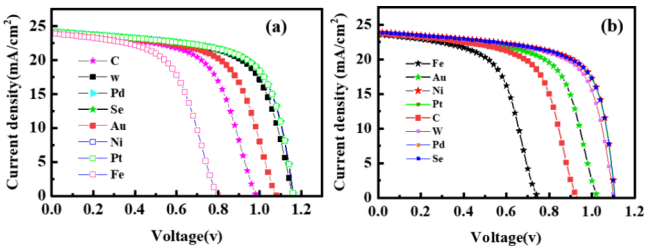

Figure 8. Perovskites current density at various metal back contacts for (a) Al-TiO_2 and (b) Mg-TiO_2.

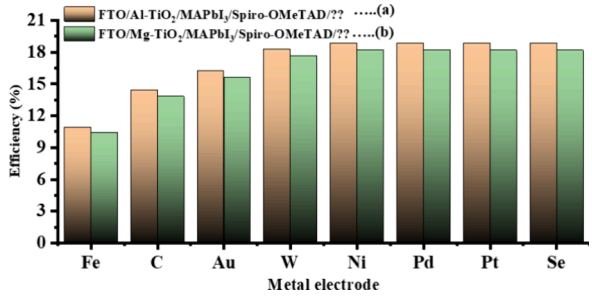

Figure 9. Perovskites efficiency at various metal back contacts for (a) Al-TiO_2 and (b) Mg-TiO_2.

structure demonstrated an optimized bandgap of 1.65 eV, while the Mg-TiO_2-based structure maintained a bandgap of 1.6 eV. To enhance the performance of both Al-TiO_2 and Mg-TiO_2 devices, optimized parameter values including thickness, operating temperature, metal electrodes, absorber doping concentrations, R_s, and R_{sh} were utilized. These optimized devices were then compared to simulated devices and validated against literature references. Table 8 presents a performance comparison between the optimized and simulated devices for V_{oc}, J_{sc}, FF, and PCE, utilizing Al-TiO_2 and Mg-TiO_2 as their respective simulated and optimized R_s and R_{sh}. In the case of Mg-TiO_2, the optimized device exhibited higher V_{oc}, J_{sc}, and FF, suggesting an increased level of electron ejection. Conversely, for Al-TiO_2, only V_{oc} and FF increased, while J_{sc} decreased, resulting in a lower PCE value of 19.26% compared to Mg-TiO_2's 19.86%. The current−voltage characteristics curves, quantum efficiency, recombination rate, and generations, as depicted in Figure 10a−d, revealed that the device performance was enhanced compared to the experimental records presented in ref 22.

4. CONCLUSIONS

Various configurations of perovskite devices were tested using experimental bandgaps of 3.2, 3.12, and 3.22 eV for TiO_2, Al-TiO_2, and Mg-TiO_2, respectively. The devices were modeled with R_s/R_{sh} values of 7.4326/330, 6.4/330, and 6.8/353 Ω cm^2 for Al-TiO_2. For Mg-TiO_2, the R_s/R_{sh} used were 6.1/201, 6.6/227, and 5.3/267 Ω cm^2, as reported in ref 31. These tests

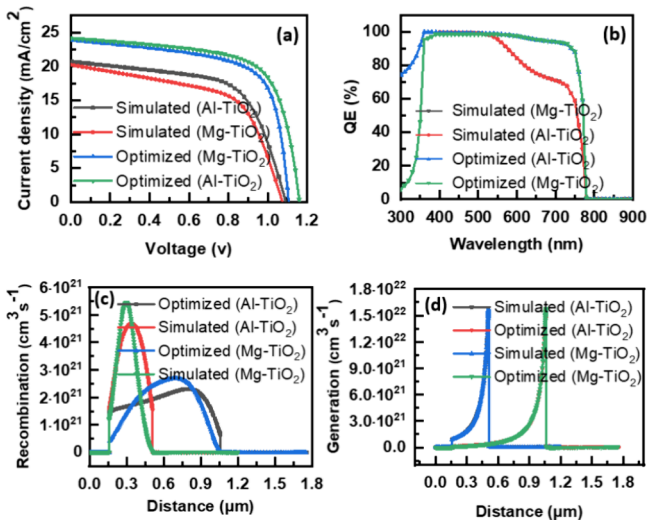

Figure 10. Overall (a) current density, (b) quantum efficiency, (c) recombination, and (d) generations rates for experimental devices and proposed simulation models of Al-TiO_2 and Mg-TiO_2.

were conducted to validate the performance closely aligned with experimental results, with a minimum percentage error at doping concentrations ranging from 0.1 to 1.0 mol % for both Al-TiO_2 and Mg-TiO_2, as presented in Table 2. The R_s and R_{sh} of 6.4/330 and 6.1/330 Ω cm^2 for Al-TiO_2 and Mg-TiO_2, respectively, with the least percentage errors, were considered as reference parameters to model the optimum device measurement. Initially, the absorber thickness was varied from 0.1 to 0.9 μm, and the optimized thickness value at the high *JV* characteristic was determined to be 0.9 μm with a minimum recombination rate. Subsequently, optimized R_s and R_{sh} values were set as default and 550 Ω cm^2 for Al-TiO_2 and Mg-TiO_2, respectively, ranging from default to 10 Ω cm^2 and 100 to 550 Ω cm^2. According to the optimized R_s and R_{sh}, the device performance was enhanced with lower R_s and higher R_{sh} values. The metal electrode at the back contact played a vital role in perovskite stability. Various metal electrodes with different work functions were tested, and some showed nearly the same performance, but Ni was found to be the most suitable electrode as reported in the literature. The optimized device has demonstrated improved performance, exhibiting a lower recombination rate compared to the simulated device validated in the literature, as shown in Table 8. This suggests that the optimized device's performance is consistent with the performance predictions for the benchmark implementation of Al-TiO_2- and Mg-TiO_2-based perovskite solar cells, utilizing all optimized parameters and Ni, identified as the most suitable electrode due to its cost-effectiveness and abundance. For future research on Al-TiO_2 and Mg-TiO_2 ETLs, it is recommended to use nontoxic, lead-free absorber layers. This would reduce toxicity, enhance stability lost due to the

Table 8. Experimental Devices and Proposed Models of Al-TiO_2 and Mg-TiO_2

configuration	measurement	V_{oc} (V)	J_{sc} (mA/cm^2)	FF (%)	PCE (%)	(R_s)	(R_{sh})
pure TiO_2	simulated model	1.100	17.250	59.460	11.320	10	254
Al-TiO_2	simulated model	1.090	20.700	61.810	13.990	6.4	330
Mg-TiO_2	simulated model	1.070	20.230	57.950	12.610	6.1	201
Al-TiO_2	optimized model	1.346	18.220	78.500	19.260	default	550
Mg-TiO_2	optimized model	1.170	23.174	72.740	19.860	default	550

https://doi.org/10.1021/acsomega.4c04505
ACS Omega 2024, 9, 39663−39672

iodine component, decrease degradation, and ensure a higher tolerance for interface defects, potentially resulting in performance improvements exceeding 20%. Consequently, this paves the way for the use of modified TiO_2 in perovskite devices to enhance charge carrier transport, conductivity, and long-term and thermal stabilities.

■ ASSOCIATED CONTENT

Data Availability Statement

The research data is publicly available throughout the manuscript and supporting file.

Supporting Information

The Supporting Information is available free of charge at https://pubs.acs.org/doi/10.1021/acsomega.4c04505.

Perovskite device performance at various absorber doping concentrations, absorber thicknesses, operating temperatures, and metal electrodes (PDF)

■ AUTHOR INFORMATION

Corresponding Author

Thiti Bovornratanaraks − *International Graduate Program of Nanoscience and Technology and Extreme Conditions Physics Research Laboratory and Center of Excellence in Physics of Energy Materials (CE:PEM), Department of Physics, Faculty of Science, Chulalongkorn University, Bangkok 10330, Thailand;* orcid.org/0000-0001-6943-4032; Email: thiti.b@chula.ac.th

Author

Abdullahi Usman − *International Graduate Program of Nanoscience and Technology and Extreme Conditions Physics Research Laboratory and Center of Excellence in Physics of Energy Materials (CE:PEM), Department of Physics, Faculty of Science, Chulalongkorn University, Bangkok 10330, Thailand;* orcid.org/0000-0002-6736-6133

Complete contact information is available at: https://pubs.acs.org/10.1021/acsomega.4c04505

Notes

The authors declare no competing financial interest.

■ ACKNOWLEDGMENTS

This research is supported by the Ratchadapisek Somphot Fund for Postdoctoral Fellowship, Chulalongkorn University. T.B. acknowledges support from Thailand Science Research and Innovation Fund Chulalongkorn University.

■ REFERENCES

(1) Mebadi, A.; Houshmand, M.; Zandi, M. H.; Gorji, N. E. Numerical Analysis of TiO_2/Cu_2ZnSnS_4 Nanostructured PV Using SCAPS-1D. *Nano Hybrids* **2014**, *8*, 27−38.

(2) Sidhik, S.; Cerdan Pasarán, A.; Esparza, D.; López Luke, T.; Carriles, R.; De La Rosa, E. Improving the Optoelectronic Properties of Mesoporous TiO2 by Cobalt Doping for High-Performance Hysteresis-free Perovskite Solar Cells. *ACS Appl. Mater. Interfaces* **2018**, *10*, 3571−3580.

(3) Teimouri, R.; Heydari, Z.; Ghaziani, M. P.; Madani, M.; Abdy, H.; Kolahdouz, M.; Asl-Soleimani, E. Synthesizing Li doped TiO2 electron transport layers for highly efficient planar perovskite solar cell. *Superlattices Microstruct.* **2020**, *145*, No. 106627.

(4) *2017 IEEE 44th Photovoltaic Specialist Conference (PVSC): 25−30 June 2017*; Institute of Electrical and Electronics Engineers: Piscataway, New Jersey, 2017.

(5) Hossain, M. K.; Ishraque Toki, G. F.; Samajdar, D. P.; Rubel, M. H. K.; Mushtaq, M.; Islam, M. R.; Rahman, M. F.; Bhattarai, S.; Bencherif, H.; Mohammed, M. K. A.; Pandey, R.; Madan, J. Photovoltaic Performance Investigation of Cs3Bi2I9-Based Perovskite Solar Cells with Various Charge Transport Channels Using DFT and SCAPS-1D Frameworks. *Energy Fuels* **2023**, *37*, 7380−7400.

(6) Hossain, M. K.; Mohammed, M. K. A.; Pandey, R.; Arnab, A. A.; Rubel, M. H. K.; Hossain, K. M.; Ali, M. H.; Rahman, M. F.; Bencherif, H.; Madan, J.; Islam, M. R.; Samajdar, D. P.; Bhattarai, S. Numerical Analysis in DFT and SCAPS-1D on the Influence of Different Charge Transport Layers of CsPbBr3 Perovskite Solar Cells. *Energy Fuels* **2023**, *37*, 6078−6098.

(7) Hossain, M. K.; Toki, G. F. I.; Kuddus, A.; Rubel, M. H. K.; Hossain, M. M.; Bencherif, H.; Rahman, M. F.; Islam, M. R.; Mushtaq, M. An extensive study on multiple ETL and HTL layers to design and simulation of high-performance lead-free CsSnCl3-based perovskite solar cells. *Sci. Rep* **2023**, *13*, No. 256811900.

(8) Lukiyanchuk, I. V.; Chernykh, I. V.; Rudnev, V. S.; Tyrina, L. M.; Ustinov, A. Y. Silicate coatings on titanium modified by cobalt and/or copper oxides and their activity in CO oxidation. *Protection of Metals and Physical Chemistry of Surfaces* **2015**, *51*, 448−457.

(9) Onozawa-Komatsuzaki, N.; Funaki, T.; Murakami, T. N.; Kazaoui, S.; Chikamatsu, M.; Sayama, K. Novel cobalt complexes as a dopant for hole-transporting material in perovskite solar cells. *Electrochemistry* **2017**, *85*, 226−230.

(10) Kim, M.; Choi, I. Woo; Choi, S. J.; Song, J. W.; Mo, S. I.; An, J. H.; Jo, Y.; Ahn, S. J.; Ahn, S. K.; Kim, G. H.; Kim, D. S. Enhanced electrical properties of Li-salts doped mesoporous TiO2 in perovskite solar cells. *Joule* **2021**, *5*, 659−672.

(11) Afriani, F.; Tiandho, Y.; Hapidin, D. A.; Dwivany, F. M.; Khairurrijal, K. Optical absorption enhancement of TiO2 via plasmonic effect of gold nanoparticles in volatile organic compounds medium. *Comput. Mater. Sci.* **2023**, *230*, No. 112462.

(12) Ishikawa, T.; Sahara, R.; Ohno, K.; Ueda, K.; Narushima, T. Electronic structure analysis of light-element-doped anatase TiO2 using all-electron GW approach. *Comput. Mater. Sci.* **2023**, *220*, No. 112059.

(13) Nishat, S. S.; Hossain, M. J.; Mullick, F. E.; Kabir, A.; Chowdhury, S.; Islam, S.; Hossain, M. Performance Analysis of Perovskite Solar Cells Using DFT-Extracted Parameters of Metal-Doped TiO2Electron Transport Layer. *J. Phys. Chem. C* **2021**, *125*, 13158−13166.

(14) Amer, M. S.; Ghanem, M. A.; Arunachalam, P.; Al-Mayouf, A. M.; Aljohani, T. A. Modification of mesoporous titanium dioxide with cobalt oxide electrocatalyst for enhanced oxygen evolution reaction. *Adv. Mater. Lett.* **2019**, *10*, 136−144.

(15) Idígoras, J.; Berger, T.; Anta, J. A. Modification of mesoporous TiO2 films by electrochemical doping: Impact on photoelectrocatalytic and photovoltaic performance. *J. Phys. Chem. C* **2013**, *117*, 1561−1570.

(16) Belošević-Čavor, J.; Koteski, V.; Umićević, A.; Ivanovski, V. Effect of 5d transition metals doping on the photocatalytic properties of rutile TiO2. *Comput. Mater. Sci.* **2018**, *151*, 328−337.

(17) Roy, S.; Botte, G. G. Perovskite solar cell for photocatalytic water splitting with a TiO2/Co-doped hematite electron transport bilayer. *RSC Adv.* **2018**, *8*, 5388−5394.

(18) Tala-Ighil Zaïr, R.; Oudjehani, C.; Tighilt, K. SCAPS Simulation for Perovskite Solar Cell. *J. Solar Energy Res. Updat.* **2021**, *8*, 21−26.

(19) Wannapop, S.; Somdee, A.; Bovornratanaraks, T. Experimental study of thin film Fe2O3/TiO2 for photocatalytic Rhodamine B degradation. *Inorg. Chem. Commun.* **2021**, *128*, No. 108585.

(20) Moura, K. F.; Maul, J.; Albuquerque, A. R.; Casali, G. P.; Longo, E.; Keyson, D.; Souza, A. G.; Sambrano, J. R.; Santos, I. M. G. TiO2 synthesized by microwave assisted solvothermal method: Experimental and theoretical evaluation. *J. Solid State Chem.* **2014**, *210*, 171−177.

(21) Ghose, K. K.; Liu, Y.; Frankcombe, T. J. Comparative First-Principles Structural and Vibrational Properties of Rutile and Anatase TiO2. *J. Phys. Condens. Matter* **2023**, *35*, 505702.
(22) Pathak, S. K.; Abate, A.; Ruckdeschel, P.; Roose, B.; Gödel, K. C.; Vaynzof, Y.; Santhala, A.; Watanabe, S. I.; Hollman, D. J.; Noel, N.; Sepe, A.; Wiesner, U.; Friend, R.; Snaith, H. J.; Steiner, U. Performance and Stability Enhancement of Dye-Sensitized and Perovskite Solar Cells by Al Doping of TiO2. *Adv. Funct Mater.* **2014**, *24*, 6046−6055.
(23) Hossain, M. K.; Rubel, M. H. K.; Toki, G. F. I.; Alam, I.; Rahman, M. F.; Bencherif, H. Effect of Various Electron and Hole Transport Layers on the Performance of CsPbI3-Based Perovskite Solar Cells: A Numerical Investigation in DFT, SCAPS-1D, and wxAMPS Frameworks. *ACS Omega* **2022**, *7*, 43210−43230.
(24) Farzaneh, A.; Javidani, M.; Esrafili, M.D.; Mermer, O. Optical and photocatalytic characteristics of Al and Cu doped TiO2: Experimental assessments and DFT calculations. *J. Phys. Chem. Solids* **2022**, *161*, No. 110404.
(25) Wang, X.; Zhang, Z.; Qin, J.; Shi, W.; Liu, Y.; Gao, H.; Mao, Y. Enhanced Photovoltaic Performance of Perovskite Solar Cells Based on Er-Yb Co-doped TiO2 Nanorod Arrays. *Electrochim. Acta* **2017**, *245*, 839−845.
(26) Liu, Y.; Zhou, W.; Wu, P. Room-temperature ferromagnetism and optical properties in Mg-doped TiO2: A density functional theory investigation. *J. Appl. Phys.* **2014**, *115*, 123913.
(27) Koketsu, T.; Ma, J.; Morgan, B. J.; Body, M.; Legein, C.; Dachraoui, W.; Giannini, M.; Demortière, A.; Salanne, M.; Dardoize, F.; Groult, H.; Borkiewicz, O. J.; Chapman, K. W.; Strasser, P.; Dambournet, D. Reversible magnesium and aluminium ions insertion in cation-deficient anatase TiO2. *Nat. Mater.* **2017**, *16*, 1142−1148.
(28) Murashkina, A. A.; Rudakova, A. V.; Ryabchuk, V. K.; Nikitin, K. V.; Mikhailov, R. V.; Emeline, A. V.; Bahnemann, D. W. Influence of the Dopant Concentration on the Photoelectrochemical Behavior of Al-Doped TiO2. *J. Phys. Chem. C* **2018**, *122*, 7975−7981.
(29) Rafieh, A. I.; Ekanayake, P.; Tan, A. L.; Lim, C. M. Effects of ionic radii of co-dopants (Mg, Ca, Al and La) in TiO2 on performance of dye-sensitized solar cells. *Sol. Energy* **2017**, *141*, 249−255.
(30) Yermakov, A. Y.; Zakharova, G. S.; Uimin, M. A.; Kuznetsov, M. V.; Molochnikov, L. S.; Konev, S. F.; Konev, A. S.; Minin, A. S.; Mesilov, V. V.; Galakhov, V. R.; Volegov, A. S.; Korolyov, A. V.; Gubkin, A. F.; Murzakayev, A. M.; Svyazhin, A. D.; Melanin, K. V. Surface magnetism of cobalt-doped anatase TiO2 nanopowders. *J. Phys. Chem. C* **2016**, *120*, 28857−28866.
(31) Rafieh, A. I.; Ekanayake, P.; Wakamiya, A.; Nakajima, H.; Lim, C. M. Enhanced performance of CH3NH3PbI3-based perovskite solar cells by tuning the electrical and structural properties of mesoporous TiO2 layer via Al and Mg doping. *Sol. Energy* **2019**, *177*, 374−381.
(32) Durodola, O. M.; Ugwu, C.; Danladi, E. Highly efficient lead-free perovskite solar cell based on magnesium-doped copper delafossite hole transport layer: a SCAPS-1D framework prospect. *Emergent Mater.* **2023**, *6*, 1665−1684.
(33) Mazumder, M. M.; Akteruzzaman, M.; Yeasmin, H.; Islam, R. Doping in TiO2 to improve solar cell efficiency: A Comprehensive Review. *ChemRxiv* **2023**.
(34) Hosseini, S. R.; Bahramgour, M.; Yardani Sefidi, P.; Tabatabaei Mashayekh, A.; Moradi, A.; Delibas, N.; Hosseini, M. G.; Niaei, A. Investigating the effect of non-ideal conditions on the performance of a planar CH3NH3PbI3-based perovskite solar cell through SCAPS-1D simulation. *Heliyon* **2022**, *8*, No. e11471.
(35) Baloch, A. A. B.; Hossain, M. I.; Tabet, N.; Alharbi, F. H. Practical Efficiency Limit of Methylammonium Lead Iodide Perovskite (CH3NH3PbI3) Solar Cells. *J. Phys. Chem. Lett.* **2018**, *9*, 426−434.
(36) Chen, Y.; Lei, Y.; Li, Y.; Yu, Y.; Cai, J.; Chiu, M. H.; Rao, R.; Gu, Y.; Wang, C.; Choi, W.; Hu, H.; Wang, C.; Li, Y.; Song, J.; Zhang, J.; Qi, B.; Lin, M.; Zhang, Z.; Islam, A. E.; Maruyama, B.; Dayeh, S.; Li, L. J.; Yang, K.; Lo, Y. H.; Xu, S. Strain engineering and epitaxial stabilization of halide perovskites. *Nature* **2020**, *577*, 209−215.
(37) Danladi, E.; Gyuk, P.M.; Tasie, N.N.; Egbugha, A.C.; Behera, D.; Hossain, I.; Bagudo, I.M.; Madugu, M.L.; Ikyumbur, J.T. Impact of hole transport material on perovskite solar cells with different metal electrode: A SCAPS-1D simulation insight. *Heliyon* **2023**, *9*, No. e16838.
(38) Raghvendra; Kumar, R. R.; Pandey, S. K. Pandey, Performance evaluation and material parameter perspective of eco-friendly highly efficient CsSnGeI3 perovskite solar cell. *Superlattices Microstruct.* **2019**, *135*, No. 106273.
(39) Danladi, E.; Egbugha, A. C.; Obasi, R. C.; Tasie, N. N.; Achem, C. U.; Haruna, I. S.; Ezeh, L. O. Defect and doping concentration study with series and shunt resistance influence on graphene modified perovskite solar cell: A numerical investigation in SCAPS-1D framework. *Journal of the Indian Chemical Society* **2023**, *100*, No. 101001.
(40) Wu, M. C.; Chan, S. H.; Lee, K. M.; Chen, S. H.; Jao, M. H.; Chen, Y. F.; Su, W. F. Enhancing the efficiency of perovskite solar cells using mesoscopic zinc-doped TiO2 as the electron extraction layer through band alignment. *J. Mater. Chem. A Mater.* **2018**, *6*, 16920−16931.
(41) Li, X.; Meng, Y.; Liu, R.; Yang, Z.; Zeng, Y.; Yi, Y.; Sha, W. E. I.; Long, Y.; Yang, J. High-Efficiency and Durable Inverted Perovskite Solar Cells with Thermally-Induced Phase-Change Electron Extraction Layer. *Adv. Energy Mater.* **2021**, *11*, No. 2102844.
(42) Sani, S.; Usman, A.; Bhatranand, A.; Jiraraksopakun, Y.; Muhammad, K.S.; Yahaya, U. A study on defect, doping, and performance of ETLs (ZnO, TiO2, and IGZO) for the lead-free CsSnCl3 perovskite solar cell by SCAPS-1D framework. *Mater. Today Commun.* **2024**, *38*, No. 107575.
(43) Ouslimane, T.; Et-taya, L.; Elmaimouni, L.; Benami, A. Impact of absorber layer thickness, defect density, and operating temperature on the performance of MAPbI3 solar cells based on ZnO electron transporting material. *Heliyon* **2021**, *7*, No. e06379.
(44) Nath, B.; Ramamurthy, P. C.; Hegde, G.; Roy Mahapatra, D. Role of electrodes on perovskite solar cells performance: A review. *ISSS J. Micro Smart Syst* **2022**, *11*, 61−79.
(45) Islam, M.S.; Sobayel, K.; Al-Kahtani, A.; Islam, M.A.; Muhammad, G.; Amin, N.; Shahiduzzaman, M.; Akhtaruzzaman, M. Defect study and modelling of SnX3-based perovskite solar cells with SCAPS-1D. *Nanomaterials (Basel)* **2021**, *11*, 1218.
(46) Hossain, M. K.; Toki, G. F. I.; Alam, I.; Pandey, R.; Samajdar, D. P.; Rahman, M. F.; Islam, M. R.; Rubel, M. H. K.; Bencherif, H.; Madan, J.; Mohammed, M. K. A. Numerical simulation and optimization of a CsPbI3-based perovskite solar cell to enhance the power conversion efficiency. *New J. Chem.* **2023**, *47*, 4801−4817.

https://doi.org/10.1021/acsomega.4c04505
ACS Omega 2024, 9, 39663−39672